ACS Catalysis

Open Access

pubs.acs.org/acscatalysis

Research Article

Synthesis, Molecular Structure, and Water Electrolysis Performance of TiO_2-Supported Raney-IrO_x Nanoparticles for the Acidic Oxygen Evolution Reaction

Jiaqi Kang, Xingli Wang, Sebastian Möhle, Shima Farhoosh, Miklós Márton Kovács, Johannes Schmidt, Liang Liang, Matthias Kroschel, Sören Selve, Michael Haumann, Dominik Dworschak, Holger Dau, and Peter Strasser*

Cite This: *ACS Catal.* 2025, 15, 5435−5446

Read Online

ACCESS | Metrics & More | Article Recommendations | Supporting Information

ABSTRACT: Developing low-cost, highly active, and stable catalysts for the acidic oxygen evolution reaction (OER) at the proton exchange membrane (PEM) water electrolyzer anodes remains a scientific priority. Reducing the iridium loading while increasing the intrinsic activity of the catalysts is essential for cost-effective hydrogen production. Here, we address a family of TiO_2-supported Raney-IrO_x catalysts with low iridium loading and high activity in single-cell PEM water electrolyzer anode environments. A controlled Raney-type Ni leaching process of pristine, supported IrNi alloy phases forms crystalline IrO_x nanoparticles (NPs) featuring metallic Ir-rich cores surrounded by more amorphous IrO_x surfaces. This structure is shown to be conducive to catalytic activity and the suppression of membrane poisoning due to Ni degradation. The trace amounts of Ni remaining after leaching in the IrO_x NPs result in heterogeneous crystal structure and induce local lattice strain. Further, we synthetically strike a balance between conductivity and activity and succeed to narrow down the notorious large performance gap between liquid electrolyte rotating disk electrodes (RDEs) and single-cell membrane electrode assembly (MEA) electrolyzer measurements. OER stability numbers (*S*-numbers) of the identified Raney-IrO_x anode catalysts surpass commercial IrO_2 catalysts, confirming the stability of these catalysts. The PEM electrolyzer tests reveal that Raney-IrO_x anodes achieve 3 A cm^{-2} at 1.8 V with a low geometric Ir loading of ca. 0.3 mg_{Ir} cm^{-2}, meeting the technically important power specific Ir utilization target of 0.05 g_{Ir}/kW.

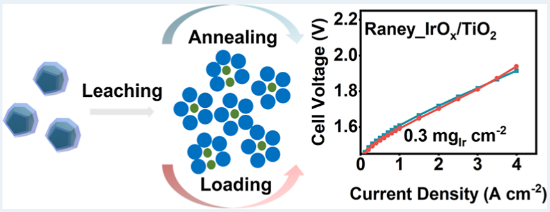

KEYWORDS: *electrolysis, iridium, oxygen evolution reaction, PEM water electrolyzer, electrocatalysis*

■ INTRODUCTION

Using environmentally friendly and sustainable energy sources, such as wind power, solar energy, and hydropower instead of fossil fuels is an inevitable "conditio sine qua non" for achieving today's net-zero emission stretch goals. However, the intermittent nature of renewable energy sources is one of the challenges to grid operators.[1−3] To solve this problem, we can use electricity generated from renewable electric technology to produce hydrogen. Then, hydrogen as an energy carrier can generate electricity through turbines or fuel cell systems.[4] Acidic proton exchange membrane (PEM) water electrolysis is a promising technology to produce low-emission green hydrogen.[2,5] However, the sluggish kinetics of oxygen evolution reaction (OER) associated with its multistep four-electron process at the anode is a bottleneck in this technique.[6,7] Iridium and iridium oxides are active state-of-the-art catalysts for the OER, yet their scarcity, hence cost, and stability may threaten wider deployment of PEM electrolyzers in the coming years.

Reducing iridium loading and increasing the intrinsic activity of the catalysts are important for cost-effective hydrogen production. Introducing non-noble metals (like Ni, Co, Cu, etc.) and using metal oxide supports are two popular approaches to achieve this goal.[8−17] Nickel is one of the most common metals to alloy with Ir as it can help to improve activity. By changing the Ir to Ni ratio, the morphology can be controlled easily.[18,19] However, non-noble metals are not stable under the OER conditions due to the harsh acidic environment and high operating potential. The dissolution of non-noble metals will poison the membrane during operation, leading to rapid degradation and an increasing cell resistance in membrane electrode assembly (MEA) tests. The contamination problem is also one of the main reasons that the results in rotating disk electrode (RDE) measurements are not comparable to MEA tests.[20,21] On the other hand, the leaching

Received: October 17, 2024
Revised: March 11, 2025
Accepted: March 11, 2025
Published: March 19, 2025

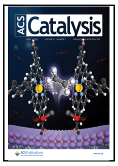

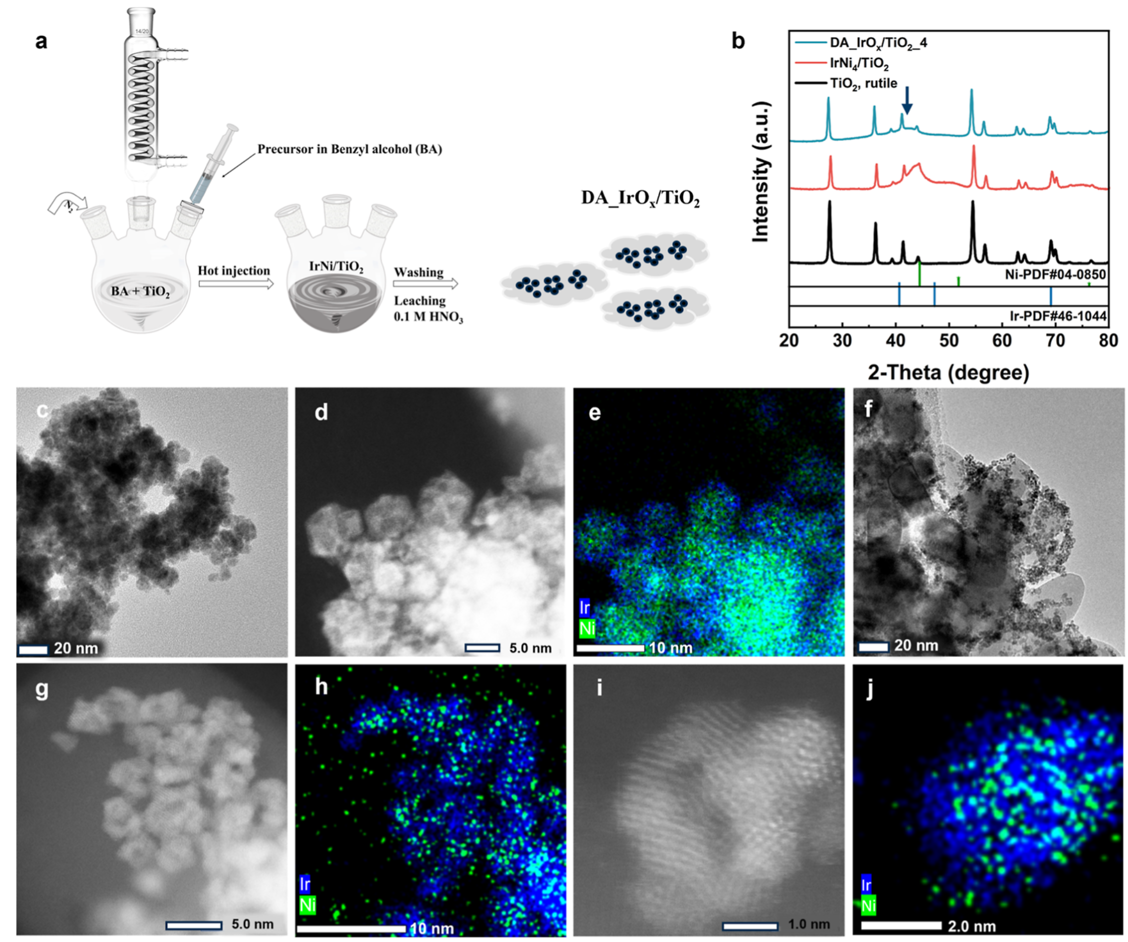

Figure 1. Synthesis and structural characterization of $IrNi_4/TiO_2$ before and after leaching. (a) Schematic of the synthesis route. (b) XRD patterns of $IrNi_4/TiO_2$ and DA_IrO_x/TiO_2_4 compared with references. (c) TEM image of $IrNi_4/TiO_2$. (d) HAADF-STEM image of $IrNi_4/TiO_2$. (e) Elemental mapping of (d). (f) TEM image of DA_IrO_x/TiO_2_4. (g,i) HAADF-STEM images of DA_IrO_x/TiO_2_4 at different scales. (h) Elemental mapping of (g). (j) Elemental mapping of (i).

of non-noble metals provides defective iridium surfaces and thus enhances the OER activity.[22] Using supports is another efficient strategy to lower the Ir loading and improve stability.[23−25] Compared to the carbon support, which is usually not stable under high potentials, Tran et al. utilized various oxides such as ATO, FTO, and ITO to support the IrNi alloy, demonstrating improved stability. However, the performance in MEA tests is still not clear.[26] Linking the activity and stability between the lab-scale RDE cell and the PEM electrolyzer is essential for future applications in the field of electrochemical engineering and renewable energy technologies.

Herein, we present a systematic investigation of both RDE and MEA electrolyzers using a novel series of TiO_2-supported IrNi nanoparticles (NPs) prepared through a facile hot injection method. The ex situ leaching process is applied to almost quantitatively remove Ni from the pristine material. This results in active and stable supported Raney-type IrO_x catalysts. The presence of nickel facilitates iridium deposition on the TiO_2 support, acting as a sacrificial template and creating NPs with improved catalytic properties. The relationship between geometric and electronic structures and catalytic performance is presented, helping to resolve the origin of the favorable kinetic performance. Further synthetic variables such as the Ir weight loading and the thermal post-treatment and their effects are investigated using X-ray photoemission spectroscopy (XPS) and X-ray absorption spectroscopy (XAS). The catalytic activity of Raney-IrO_x catalysts reaches 324 A g_{Ir}^{-1} at 1.53 V vs RHE, marking an increase by a factor of 4 over commercial IrO_2 from Alfa Aesar (IrO_2_AA) and by a factor of 34 when compared to the commercial TiO_2 supported rutile IrO_2 catalyst (Umicore). Unlike most previous studies, we address the performance of the new catalysts in liquid RDE cells and in PEM electrolyzer cells. To reduce the differences between RDE and MEA electrolyzers, we take conductivity into consideration. Our balance between conductivity, activity, and stability helps narrow down the gap between RDE and MEA measurements. Favorable stability numbers (*S*-numbers) for selected Raney-IrO_x catalysts are reported and the technical Ir utilization target of 0.05 g_{Ir}/kW is met in PEM single cell tests.

■ RESULTS AND DISCUSSION

Synthesis and Characterizations. Figure 1a illustrates the synthesis route, which includes hot-injection and acid leaching steps. TiO_2-supported IrNi was initially synthesized by using the hot-injection method. First, Ir and Ni precursors were dissolved in benzyl alcohol (BA) at 60 °C. This solution was then injected into a separate BA solution containing TiO_2 at 160 °C and was reacted for 4 h under continuous stirring.

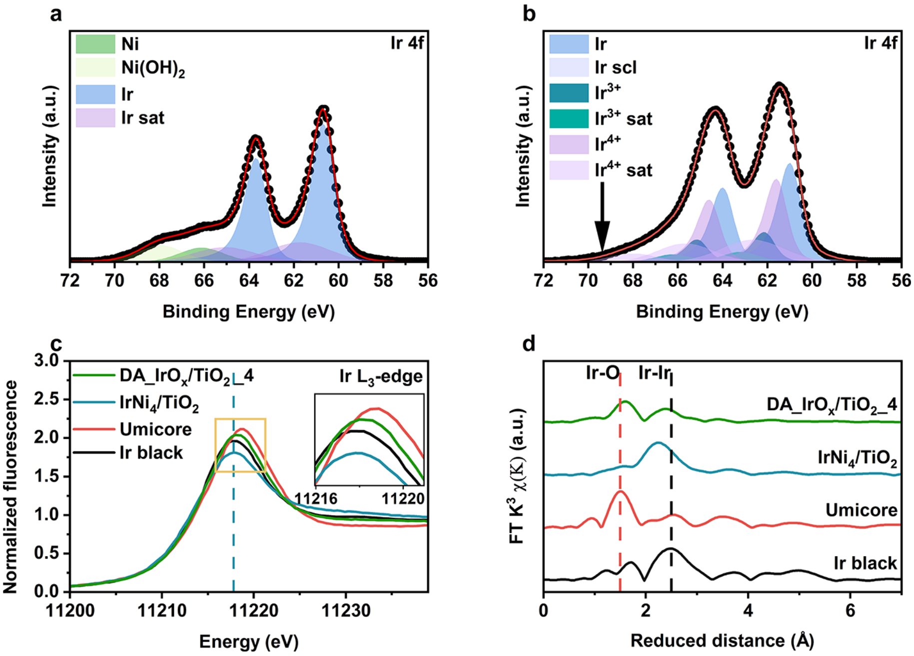

Figure 2. Electronic structures of IrNi$_4$/TiO$_2$ and DA_IrO$_x$/TiO$_2$_4. (a) XPS spectrum of Ir 4f and Ni 3p of IrNi$_4$/TiO$_2$. (b) XPS spectrum of Ir 4f and Ni 3p of DA_IrO$_x$/TiO$_2$_4. (c) XANES spectra at the Ir L$_3$-edge of IrNi$_4$/TiO$_2$ and DA_IrO$_x$/TiO$_2$_4 compared to Ir black (metal) and Umicore (IrO$_2$/TiO$_2$). (d) Respective k^3-weighted FT-EXAFSEXAFS spectra (for *k*-space data and EXAFS simulation results see Figure S10 and Table S5).

The resulting products were leached in 0.1 M HNO$_3$ for 12 h at room temperature (further details are provided in the Methods). The synthesized catalyst is referred to as IrNi$_y$/TiO$_2$ before leaching, DA_IrO$_x$/TiO$_2$_*y* after leaching, and DA_IrO$_x$/TiO$_2$_*y*_*T* after leaching and annealing, where "*y*" represents the initial molar ratio of Ni to Ir, and "*T*" denotes the annealing temperature (°C). All Ir loadings are 40 wt % after leaching unless noted otherwise. The powder X-ray diffraction (XRD) patterns (Figures 1b and S6) display a distinct reflection from the (111) facet of metallic IrNi (marked by an arrow), confirming the formation of disordered alloy phases between Ir and Ni. Then DA_IrO$_x$/TiO$_2$_*y* with negligible Ni content (Ni to Ir atomic ratios were all around 0.2) was obtained after leaching. The leaching process led to a reduction in the reflection intensity of (111) facet and a shift to lower values, indicating that the IrNi NPs were dealloyed. The peak position of the IrNi NPs after leaching was similar to that of metallic Ir. All the Ir and Ni weight loadings were determined by X-ray fluorescence (XRF) spectroscopy (Figures S1 and Table S1). An Ir weight loading of 40 wt % was targeted after leaching to ensure conductivity.[27] An Ni/Ir atomic ratio of 2 was required to achieve the expected Ir loading. This may be due to changes in particle size, which alter the surface zeta potential within the reaction system.[28] It shows that the particle size increased from IrNi$_2$ to IrNi$_4$ with increasing Ni to Ir atomic ratios based on transmission electron microscopy (TEM) (Figures 1c and S2). The results from the TEM images were consistent with the changes in Ir loading. Both TEM images and scanning electron microscopy (SEM) elemental mappings of IrNi$_4$/TiO$_2$ indicated that IrNi NPs are loaded onto TiO$_2$ (Figure S3), demonstrating the successful synthesis of TiO$_2$-supported IrNi NPs. After leaching, the NPs were still on TiO$_2$ and the size of NPs changed during the dealloying procedure (Figures 1f, S4 and S5). The IrO$_x$ NPs in DA_IrO$_x$/TiO$_2$_4 had the smallest size compared to those in DA_IrO$_x$/TiO$_2$_2 and DA_IrO$_x$/TiO$_2$_3. The morphology of the IrNi$_4$/TiO$_2$ and DA_IrO$_x$/TiO$_2$_4 was further revealed by high-angle annular dark-field scanning TEM (HAADF-STEM) (Figures 1d,e,g−j and S7). HAADF-STEM image and energy dispersive X-ray (EDX) analysis demonstrated that IrNi NPs have a core−shell structure, which is also consistent with the XRD results. It shows that the IrNi NPs have a Ni-rich core and Ir-rich surface. We measured the atomic ratio of IrNi$_4$/TiO$_2$ with XRF and XPS. The different results between XRF (Ni to Ir atomic ratio was 4.34) and XPS (Ni to Ir ratio was 2.47) also confirmed that IrNi$_4$/TiO$_2$ has an Ir-rich surface, since XPS is more surface sensitive (Tables S1 and S2). Elemental mappings and HAADF-STEM images of DA_IrO$_x$/TiO$_2$_4 showed that most Ni atoms in IrNi$_4$/TiO$_2$ were leached out, transforming the IrNi core−shell structure into small crystalline Ir NPs with a heterogeneous crystal structure (Figure 1g−j,b). DA_IrO$_x$/TiO$_2$_4 had an average particle size of 2.33 ± 0.76 nm, which was consistent with the XRD results. The crystalline Ir NPs suggest enhanced stability in OER.[29,30]

Electronic Structural Characterizations. To explore the changes in the electronic structure and coordination environment after leaching, XPS and XAS measurements were executed. XPS peak fittings were done to determine the surface species of Ir and Ni (detailed information can be seen in Table S4). The Ir 4f spectrum exihibts three sets of doublets at 60.6 and 63.6, 62.5 and 64.5, 61.6 and 64.6 eV, which can be assigned to metallic Ir, Ir^{3+}, and Ir^{4+}.[31] Figure 2a shows the Ir 4f and Ni 3p spectrum of IrNi$_4$/TiO$_2$. It showed that Ir was mainly metallic Ir. Ni exhibited both metallic Ni and Ni^{2+} species, which might be due to partial oxidation in air. After leaching, the Ni 3p peak in the XPS spectra disappeared (Figure 2b). Ni 2p peaks also showed lower intensity after leaching compared to that of IrNi$_4$/TiO$_2$ (Figure S8a,b). The overall Ir 4f peak shifted to higher binding energy,

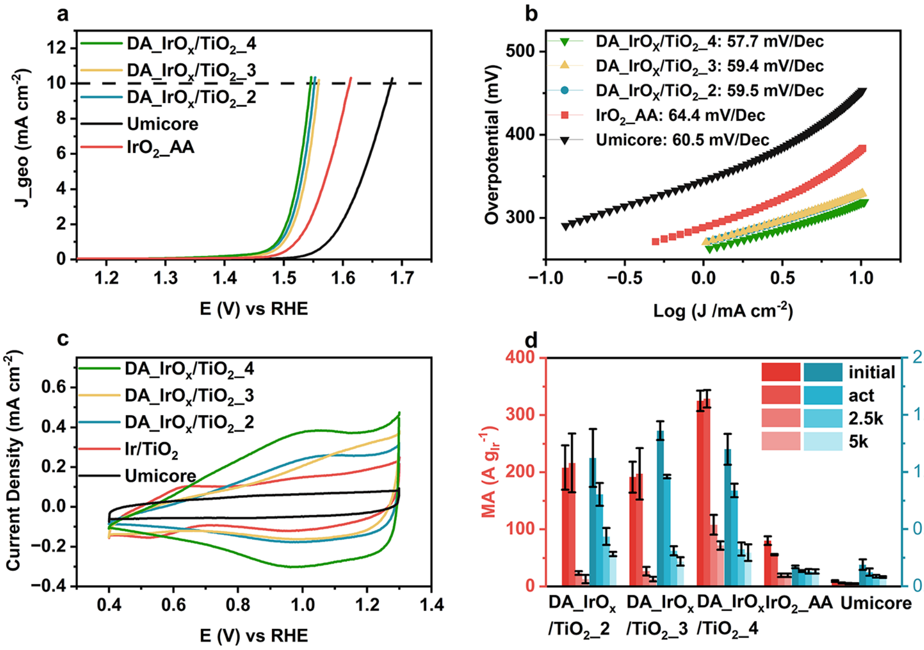

Figure 3. Electrochemical characterization of DA_IrO$_x$/TiO$_2$ with different Ni to Ir ratios. (a) Polarization curves. (b) Tafel plots. (c) Cyclic voltammograms (CVs). (d) MA and SA changes during ASTs at 1.53 V vs RHE. All the results are *iR*-compensated and the measurements are performed in N$_2$-saturated 0.05 M H$_2$SO$_4$ electrolyte. Ir loading on the gold electrode is 17.8 μg_{Ir} cm^2.

demonstrating an increase in the oxidation states of Ir. Deconvolution of the Ir 4f peaks indicated that Ir in DA_IrO$_x$/TiO$_2$_4 exhibited a mixed oxidation state of Ir^{3+} (peaks at 62.1 and 65.1 eV), Ir^{4+} (peaks at 61.6 and 64.6 eV) and Ir^0 (peaks at 60.9 and 63.9 eV). The shift in the Ir 4f peaks suggested that the surfaces of the Ir NPs were oxidized during the dealloying process, likely forming hydroxyl groups on the amorphous surface evident by the presence of Ir^{3+}.[31] The XPS spectra of O 1s also showed an increased intensity in DA_IrO$_x$/TiO$_2$_4 due to oxidation (Figure S8c,d). Ir 4f and Ni 3p spectra of catalysts with different Ni to Ir atomic ratios before and after leaching were also obtained (Figure S9). They all showed similar changes after leaching. The changes in XPS spectra confirmed that the leaching process oxidized the surface of the NPs and provided surface hydroxyl groups and might have resulted in lattice oxygen vacancies, which would benefit the OER performance. Ir L$_3$-edge X-ray absorption near edge structure (XANES) spectra also indicated that IrNi$_4$/TiO$_2$ had a similar Ir L$_3$-edge white line peak energy position to Ir black, whereas DA_IrO$_x$/TiO$_2$_4 had a slight shift to higher energy, suggesting a higher oxidation state compared to metallic Ir (Figure 2c). XANES results were in agreement with the XPS spectra, which indicated the existence of IrO$_x$. After leaching, the oxidation state of Ni also increased due to the oxidizing of Ni (Figure S11a,b). The Fourier transforms (FTs) of the extended X-ray absorption fine structure (EXAFS) spectra provided crucial information about the bond lengths in the catalysts. Figure 2d displays the Ir L$_3$-edge k^3-weighted FT-EXAFS spectra, while the corresponding simulation results are detailed in Figure S10 and Table S5. In the IrNi$_4$/TiO$_2$ catalyst, the main metallic peak between 2 and 3 Å can be deconvoluted into contribution from two distinct bonds. Both metal−metal bonds, with bond lengths of 2.55 and 2.62 Å, were shorter than the Ir−Ir bond in Ir black (2.69 Å) but longer than the Ni−Ni bond in Ni metal (2.49 Å). These variations in bond length are attributed to the incorporation of nickel into the iridium structure.[32] The presence of two different metallic bonds indicated that the IrNi NPs in IrNi$_4$/TiO$_2$ consist of an Ir-rich shell with longer metal−metal bonds and a Ni-rich core with shorter metal−metal bonds. Ni K-edge EXAFS data were also fitted, with the spectra and simulation results presented in the Supporting Information (Figure S11c,d, and Table S6). In addition to the Ni−Ni bond (2.50 Å), the presence of the Ni−Ir bond with a bond length of 2.65 Å further confirms the core−shell structure. Changes in the FT-EXAFS spectra after leaching reflected variations in the Ir oxide and metallic Ir contributions. It showed an increase in Ir oxide contributions in DA_IrO$_x$/TiO$_2$_4. The Ir−Ir bond length was determined to be 2.60 Å, indicating that most of the Ni was leached out. The peak of the Ni−Ni bond also disappeared, leaving only the Ni−Ir bond (2.62 Å) based on the FT-EXAFS spectra at the Ni K-edge. Combining with the XRD patterns and HRTEM images, this analysis suggests that the presence of trace amounts of Ni in the IrO$_x$ NPs alters the structure of metallic Ir in the core, potentially inducing a strain effect. Compared to the bond length of Ir−O in the rutile Umicore catalysts (1.95 Å), the Ir−O bond in DA_IrO$_x$/TiO$_2$_4 was slightly longer at 2.03 Å, suggesting weaker covalency of Ir−O in Raney-IrO$_x$ within DA_IrO$_x$/TiO$_2$_4.[33] Furthermore, the hydroxyl group on the surface of the amorphous IrO$_x$ contributes to longer Ir−O bond lengths, which could experimentally result in lower OER overpotential.[34]

Acidic OER Performance in RDE. The electrochemical performance was measured by using a three-electrode cell in N$_2$-saturated 0.05 M H$_2$SO$_4$. With an increase in the Ni/Ir ratio, the activity of the as-prepared catalysts decreased, as illustrated in Figure S12. However, the as-prepared catalysts were not stable due to Ni degradation and were not suitable for cell measurements. After leaching, only trace amounts of Ni were left, based on XRF, XPS, and EDX mappings (Tables S1−S3). As shown in Figure 3a, DA_IrO$_x$/TiO$_2$_4 had the

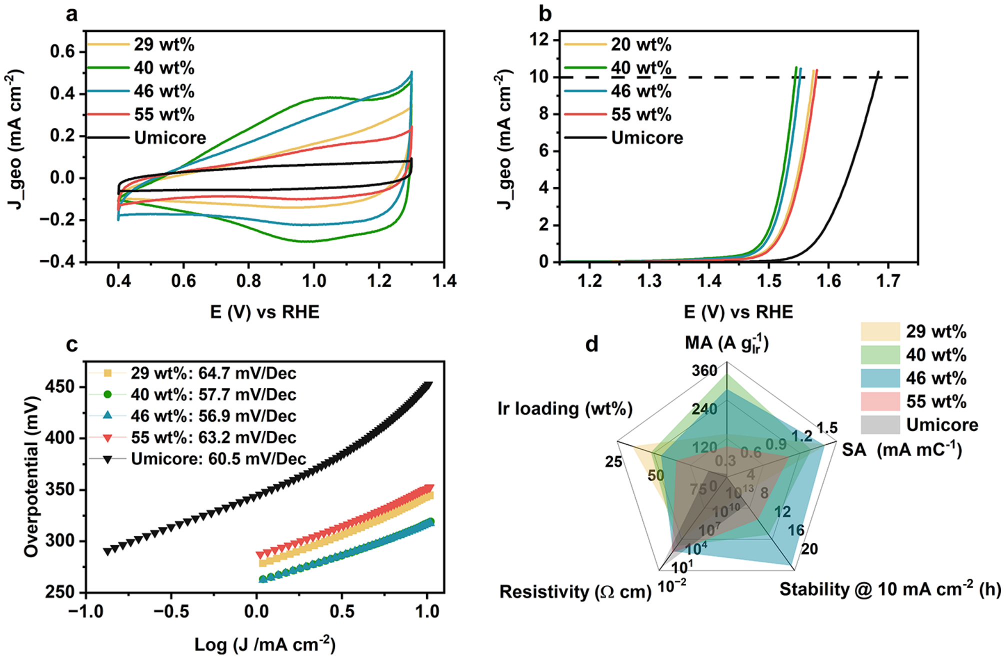

Figure 4. Electrochemical characterization of DA_IrO_x/TiO_2_4 with different Ir loadings. (a) CVs. (b) Polarization curves. (c) Tafel plots. (d) Spider diagram depicting the correlations of electrochemical and physical properties: resistivity (measured at 290 MPa), Ir loading, MA, and SA at 1.53 V vs RHE and durability at a constant current density of 10 mA cm^{-2}.

best OER activity. The Tafel slope of DA_IrO_x/TiO_2_4 was 57.7 mV/dec, the smallest among both the as-synthesized and commercial catalysts, indicating a lower activation energy barrier for the OER and faster kinetics (Figure 3b). All leached catalysts showed similar Tafel slopes and were consistent with previously reported values of Ir-based catalysts.[35] Tafel analysis suggested that the adsorption of hydroxyl groups on the catalyst surface is the rate-determining step of the OER.[36,37] The similar kinetic behavior observed in comparison to IrO_2 also indicates that the surfaces of DA_IrO_x/TiO_2 are oxide layers, consistent with previous studies and the XPS results shown in Figure 2b.[38] The charge between 0.4 and 1.3 V vsRHE was proportional to the electrochemically active surface area, which we used to calculate the specific activities.[39] In Figure 3c, DA_IrO_x/TiO_2_4 had the largest charge between 0.4 and 1.3 V vs RHE due to the small sizes of IrO_x NPs. All leached catalysts displayed a distinct peak in this region, indicating the formation of Ir^{4+}. It suggested that Ir in the leached catalysts behaved more like metallic Ir although the surfaces were oxidized. We could interpret that the amorphous IrO_x shell was very thin, therefore, the activation step was crucial to obtain fully oxidized surface. DA_IrO_x/TiO_2_4 had a mass activity (MA) of 324 A g_{Ir}^{-1} at 1.53 V vs RHE, which was 3 times higher than IrO_2_AA and 33 times higher than that of Umicore. The MA showed almost no change after activation (Figure 3d), suggesting that almost no Ni dissolution happened. The MA of DA_IrO_x/TiO_2_4 was superior to those of some reported supported catalysts (Table S7). The specific activities (SAs) of as-synthesized catalysts had higher SA and MA values compared to commercial catalysts, indicating higher intrinsic activities of as-synthesized catalysts (Table S8). Using Ni as a template and doping element to produce TiO_2 supported surface amorphous and inner crystalline IrO_x NPs with high OER activity was proven to be a superior synthesis strategy. Even after 5000 accelerated stress test (AST) cycles of square wave voltammetry (SWV) between 0.6 V vs RHE and 1.6 V vsRHE, it still displayed an MA of 100 A/g_{Ir}, which was higher than the initial activities of the commercial catalysts (Figure 4d). DA_IrO_x/TiO_2_4 was considered to be the most stable catalyst among all catalysts with different initial Ni to Ir ratios (Figure S13).

Balancing the Activity, Stability, and Conductivity for MEA Measurements. To achieve a comparable performance in MEA measurements, we changed the iridium weight loadings of DA_IrO_x/TiO_2_4. DA_IrO_x/TiO_2_4 with different Ir loadings were obtained by changing the initial precursor inputs. The TEM images indicated variations in the loadings of NPs on TiO_2 based on different precursor inputs, as shown in Figure S14. As the iridium weight loading increased, the active surface area increased first and then decreased when the loading reached 55 wt % (Figure 4a). The Tafel slope had only a slight change by changing the loading of iridium on TiO_2, suggesting that they share the same kinetic pathway (Figure 4c). DA_IrO_x/TiO_2_4 with an Ir loading of 40 wt % had the highest activity shown in Figure 4b and DA_IrO_x/TiO_2_4 with an Ir loading of 46 wt % showed comparable activity. The spider diagram in Figure 4d provides a detailed comparison of catalysts with varying Ir loadings. In terms of stability, the TEM images of DA_IrO_x/TiO_2_4 with Ir loading of 46 wt % showed no significant aggregation or dissolution of IrO_x NPs after 5000 AST cycles (Figure S15a). It remained stable at 10 mA cm^{-2} for 20 h and exhibited the smallest overpotential shift after AST (Figure S16). Higher Ir loading reduced the catalyst's resistivity.[40] DA_IrO_x/TiO_2_4 with an Ir loading of 46 wt % exhibited a resistivity of approximately 10 Ω cm at 290 MPa, as measured by our homemade setup (Figures S17 and S18), making it optimal for MEA measurements.[41] Additionally, DA_IrO_x/TiO_2_4 with Ir loading of 46 wt % achieved an MA of 273 A g_{Ir}^{-1} at 1.53 V vsRHE and had the highest SA of 1.36 mA mC^{-1}. Overall, an Ir loading of 46 wt % was determined to be the optimal loading for DA_IrO_x/TiO_2_4 in MEA measurements.

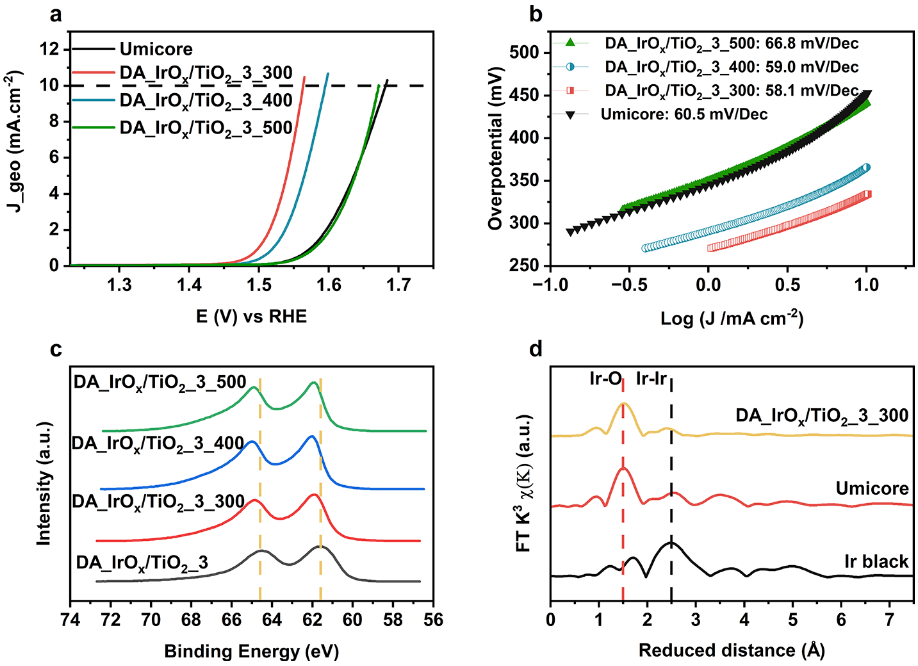

Figure 5. Electrochemical characterization and electronic structures of DA_IrO$_x$/TiO$_2$_3 and DA_IrO$_x$/TiO$_2$_3 after annealing in air at different temperatures for 1 h. (a) Polarization curves. (b) Tafel plots. (c) XPS spectra of Ir 4f. (d) k^3-weighted FT-EXAFS spectra of DA_IrO$_x$/TiO$_2$_3_300 and references at the Ir L$_3$-edge.

In order to achieve highly conductive and stable catalysts, an alternative approach for optimizing the catalysts was to perform post-annealing of the leached catalysts in air. Conductivity is a crucial factor for catalysts in real PEM electrolyzer operations, enabling efficient electron transport through thicker catalyst layers compared with RDE setups. It also helps reduce resistance, particularly at the interface between the anode catalyst and the porous transport layer (PTL).[42] The annealing process was determined to be an effective method for enhancing the crystallinity of the catalysts, ultimately resulting in the production of highly conductive and stable catalysts.[43] DA_IrO$_x$/TiO$_2$ catalysts were annealed in air at 300 °C for 1 h. TEM images showed that the sizes of the IrO$_x$ NPs increased after annealing (Figure S19a−c). The XRD patterns of annealed catalysts also had amorphous Ir oxide peaks like in IrO$_2$_AA (Figure S20b). After annealing, DA_IrO$_x$/TiO$_2$_3 showed the highest activity of 187 A g_{Ir}^{-1} at 1.53 V vs RHE, and the stability was also increased, with no obvious changes in the TEM image after 5000 AST cycles (Figures S21 and S15b). The relatively large particle size of IrO$_x$ in DA_IrO$_x$/TiO$_2$_3 might contribute to the greater stability during the annealing process. To optimize the annealing temperature, the catalysts were annealed at 300, 400, and 500 °C, respectively. The sizes of IrO$_x$ NPs increased with increasing annealing temperature due to sintering, which was confirmed in both TEM images. Additionally, the crystallinity increased as well based on XRD patterns. The changes observed due to annealing were consistent with findings from previous studies (Figures S19d,e and S20c).[43] Nevertheless, an increased degree of crystallization also resulted in an elevated conductivity. As shown in Figure 5a,b, when the annealing temperature reached 400 °C, sintering of the NPs resulted in decreased activity, accompanied by an increase in the Tafel slope. This indicates higher activation energy barriers and suggests that the OER occurring on the catalyst surfaces is less kinetically favorable than DA_IrO$_x$/TiO$_2$_3_300. However, the conductivity of the catalysts increased (Figure S22). To know more about the annealing effect on the electronic structure, XPS and XAS measurements were also performed. From XPS spectra of Ir 4f, we observed that the peaks shifted to higher binding energies with increasing annealing temperatures, indicating an increase in the oxidation states of Ir (Figures 5c and S23). The FT-EXAFS spectrum of DA_IrO$_x$/TiO$_2$_3_300 at the Ir L$_3$-edge in Figures 5d and S10d revealed that NPs in DA_IrO$_x$/TiO$_2$_3_300 had an Ir−O distance of 1.96 Å, which was closer to that of rutile IrO$_2$ in Umicore (Table S6). The XANES spectrum of DA_IrO$_x$/TiO$_2$_3_300 at the Ir L$_3$-edge showed that the oxidation state of Ir was near Ir^{IV}, consistent with the EXAFS results (Figure S24). Additionally, the XANES spectrum of DA_IrO$_x$/TiO$_2$_3_300 at the Ni K-edge (Figure S11b) confirmed that the Ni inside was also fully oxidized with a similar Ni−O bond length (2.04 Å) compared to NiO (2.07 Å) (Table S6). Considering the balance between conductivity and RDE performance, DA_IrO$_x$/TiO$_2$_3_300 was identified as one of the most suitable catalysts for MEA measurements.

MEA and Online ICP−MS Measurements. MEA measurements were carried out at 80 °C under ambient pressure using a commercial test station to assess the catalytic performance of the OER across different electrolyte environments, ranging from idealized liquid electrolyte RDE conditions to realistic PEM electrolyzer anode environments. The cell setup is shown in Figure S25. DA_IrO$_x$/TiO$_2$_4 after optimization had a loading of 46.3 wt %. Both DA_IrO$_x$/TiO$_2$_4 and DA_IrO$_x$/TiO$_2$_3_300 achieved similar performances compared to commercial IrO$_2$/TiO$_2$ from Umicore, but with a lower loading of around 0.3 mg$_{Ir}$ cm^{-2} (Figure 6a). In Figure 6c, DA_IrO$_x$/TiO$_2$_4 showed the highest MA at 1.58 V, with an MA of 3042.3 A g^{-1}. DA_IrO$_x$/TiO$_2$_4 reached a potential of 1.81 V at 3 A cm^{-2}, while DA_IrO$_x$/TiO$_2$_3_300 had a potential of 1.82 V at 3 A cm^{-2}. Both catalysts had higher high frequency resistances (HFR) than Umicore. DA_IrO$_x$/

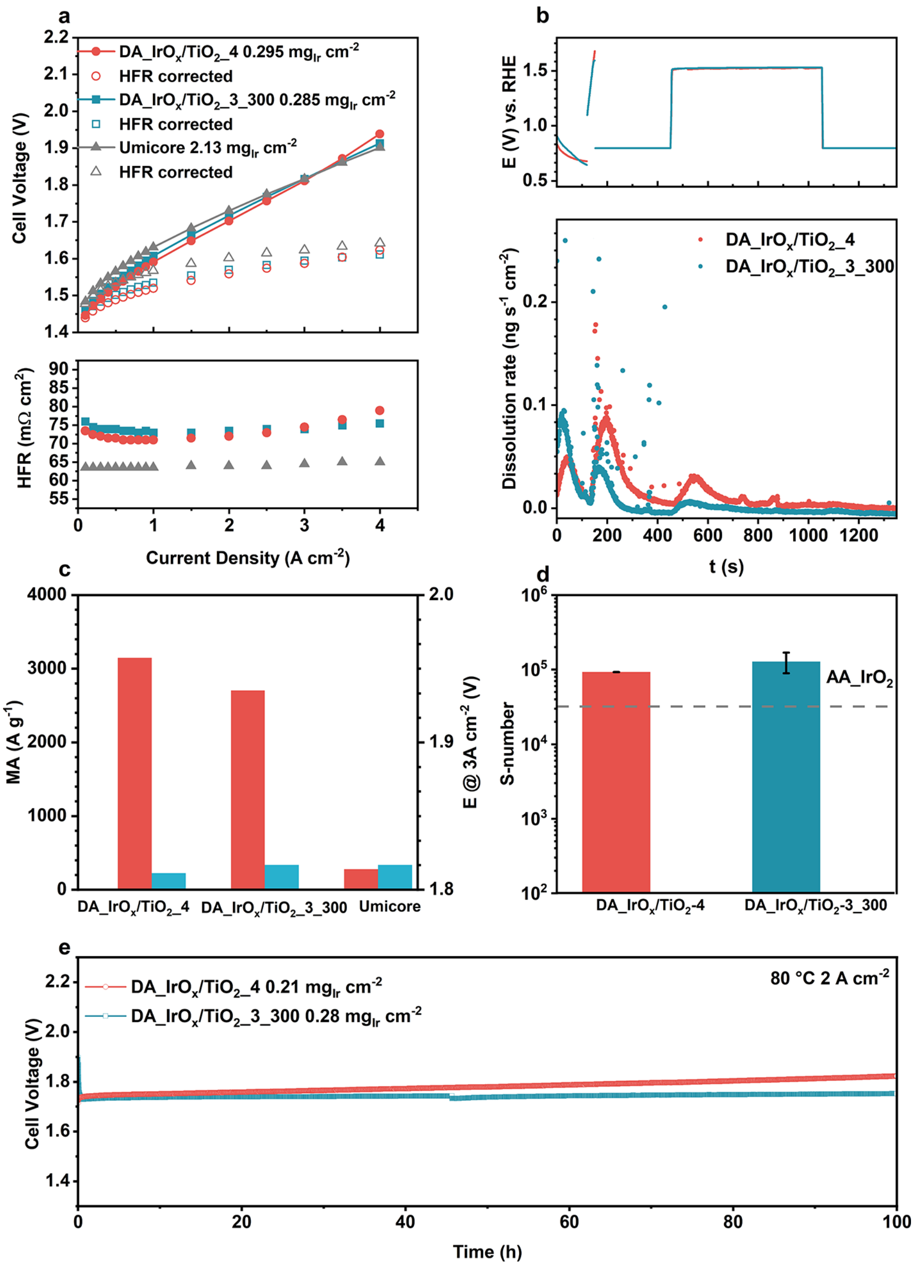

Figure 6. Activity and stability of optimized catalysts. (a) Polarization curves and corresponding HFR in MEA at 80 °C with Nafion 212. (b) Online ICP−MS measurements for the dissolution of iridium. (c) MA at 1.58 V and voltage at 3 A cm^{-2}. (d) *S*-numbers obtained from holding a constant current at 1 mA cm^{-2}. (e) Chronopotentiometric measurements of DA_IrO_x/TiO_2_4 and DA_IrO_x/TiO_2_3_300.

TiO_2_4 has a slightly larger HFR than DA_IrO_x/TiO_2_3_300. Although DA_IrO_x/TiO_2_4 showed twice the MA of DA_IrO_x/TiO_2_3_300 in RDE measurements, their conductivity of DA_IrO_x/TiO_2_3_300 was 10 times higher than DA_IrO_x/TiO_2_4. The conductivity difference also played an important role in the cell test. Measurements using scanning flow cell (SFC) coupled with inductively coupled plasma mass spectrometry (ICP−MS) showed the dissolution of Ir, Ni, and Ti during potential ramping and under galvanostatic conditions (Figures S26−S28). In Figure 6b, the Ir dissolution rate of DA_IrO_x/TiO_2_4 was higher than that of DA_IrO_x/TiO_2_3_300, suggesting that the pronounced presence of hydrous hydroxyl groups on the surface of IrO_x could lead to instability and reconstruction of the surface during the OER. However, it will be stable after the surface is fully oxidized. Ni dissolution rate was high due to the fast leaching of unstable Ni ions, which can be seen in EDX mapping in Figure 1. Ti had almost no dissolution in both catalysts. Figure 6d summarizes the *S*-numbers of these two catalysts under different conditions. They both had *S*-numbers above 10^4, which were slightly higher than IrO_2_AA based on reported value.[10,44] Additionally, we conducted 100 h of MEA stability tests for both catalysts (Figure 6e). DA_IrO_x/TiO_2_3_300 demonstrated greater stability than DA_IrO_x/TiO_2_4, consistent with their *S*-numbers. The degradation for DA_IrO_x/TiO_2_3_300 primarily attributed to ohmic losses from membrane degradation, while for DA_IrO_x/TiO_2_4, the HFR-free activity also decreases during tests (Figure S29). Figure S30 presents the EDX spectra for the anode side and membrane after the stability tests. The presence of Ni in the membrane suggests that even a small amount of Ni leaching may contribute to membrane degradation. This effect is minimal compared to typical cationic-impurities-induced Ohmic losses, as only trace amounts of Ni are in the catalysts.[45] A 100 h cell test is not typically considered effective for evaluating the stability in PEM water electrolyzers. Therefore, long-term stability tests (≥1000 h) are planned for future work.[46,47] The Ir utilization values summarized in Figure S31 indicate that both DA_IrO_x/TiO_2_4 and DA_IrO_x/TiO_2_3_300 achieved a power specific Ir utilization of ca. 0.05 g_{Ir}/kW at 3 A cm^{-2} (around 70% of the lower heating value). This value achieves the technical PEM electrolysis development threshold of 0.05 g_{Ir}/kW reported previously. With this target, both catalysts meet the 2035 target for hydrogen production.[2,48]

CONCLUSIONS

In conclusion, we offer a detailed and comprehensive synthesis-structure−performance analysis of new low-iridium-weight OER anode catalysts for PEM water electrolyzers. This study encompasses fundamental material synthesis aspects and extends to performance analyses at the electrolyte cell level.

We report a facile method for obtaining TiO_2 supported IrO_x NPs with a low Ir loading using Ni as a template and a doping element. By varying the initial Ni to Ir ratios, we can alter the morphologies of the IrO_x NPs. The leaching step not only removes the Ni template, resulting in highly crystalline and stable TiO_2-supported Raney-IrO_x, but also enriches the amorphous surfaces of Ir NPs with hydroxyl groups, thereby enhancing their activity. The heterogeneous crystal structure in IrO_x NPs, resulting from trace amounts of Ni, induces local lattice strain, leading to more stable and active catalysts.[49] To further optimize the catalysts, we adjust the Ir loading and apply post-annealing treatment. DA_IrO_x/TiO_2_4 and DA_IrO_x/TiO_2_3_300 reach a current density of 3 A cm^{-2} around 1.8 V with a significantly low Ir loading of 0.3 mg_{Ir} cm^{-2} in MEA test. This amounts to a power-specific Ir utilization of 0.05 g_{Ir}/kW. The Ir loadings in these catalysts are also low (46.3 and 38 wt %) compared to commercial catalyst from Umicore, which typically contains 75 wt % Ir. Online ICP−MS and chronopotentiometric measurements indicate that DA_IrO_x/TiO_2_4 and DA_IrO_x/TiO_2_3_300 exhibit potential long-term stability for PEM water electrolyzers with low Ir loadings. However, the effects of trace amounts of Ni on the activity and membrane degradation still need to be considered. This study offers a more complete pathway for designing Ir-based catalysts for PEM water electrolyzers, helping to bridge the gap between RDE and MEA measurements.

METHODS

Chemicals and Materials. Iridium acetate ($Ir(OAc)_3$) was purchased from Chempur, nickel acetylacetonate ($Ni(acac)_2$), and iridium dioxide (IrO_2) were purchased from Alfa Aesar, Elyst Ir75 (IrO_2/TiO_2) and Elyst Pt50 (Pt/C) were purchased from Umicore, Ir black was purchased from Fuel Cell Store, titanium oxide (TiO_2, rutile) and Nafion solution (5% w/w) were purchased from Sigma-Aldrich, benzyl alcohol (BA, ≥99%) was purchased from Carl Roth, ethanol, isopropanol, sulfuric acid (H_2SO_4, min 95%), and nitric acid (HNO_3, 63%) were purchased from VWR International. All chemicals were used as received.

Materials Preparation. The synthesized catalyst samples will be referred to as $IrNi_y/TiO_2$ before leaching, DA_IrO_x/TiO_2_*y* after leaching, and DA_IrO_x/TiO_2_*y*_*T* after leaching and annealing, where "*y*" represents the initial molar ratio of Ni to Ir, and "*T*" denotes the annealing temperature (°C). The final weight loading will be noted in parentheses if it is necessary.

$IrNi_y/TiO_2$. $IrNi_y/TiO_2$ was synthesized by using the hot-injection method. For instance, to prepare $IrNi_4/TiO_2$ with an expected 40 wt % Ir loading postleaching, 90 mg of TiO_2 was added to 130 mL BA in a glass reactor. After dispersion with ultrasonication for 15 min, the glass reactor was heated to 160 °C under nitrogen flow. In parallel, 0.5 mmol of $Ir(OAc)_3$ and 2.0 mmol of $Ni(acac)_2$ were added in 20 mL BA and the mixture was heated to 60 °C and kept at that temperature for 1 h under stirring. Once the precursors dissolved completely in BA, they were injected into the glass reactor at 160 °C, where the reaction was maintained for 4 h before cooling to room temperature (RT). The final products were collected and washed with ethanol three times by centrifugation and then were freeze-dried. For other desired Ni to Ir atomic ratios of 1, 2, and 3, the initial amounts of Ni precursor were changed accordingly. For different Ir loadings, the initial amounts of TiO_2 were changed accordingly.

DA_IrO_x/TiO_2_y. 100 mg $IrNi_y/TiO_2$ was dispersed in 50 mL of 0.1 M HNO_3 aqueous solution and stirred for 12 h. The products were collected by centrifugation and then washed to a neutral pH with Milli-Q water. The final powders were dried by freeze-dryer.

DA_IrO_x/TiO_2_y_T. In a typical synthesis of DA_IrO_x/TiO_2_3_300, 30 mg of DA_IrO_x/TiO_2_3 was annealed in a muffle furnace at 300 °C for 1 h at a heating rate of 5 °C/min. To compare effects, the annealing temperature was varied to 400 and 500 °C.

Physical Characterization. XRD measurements were performed using a D8 ADVANCE Diffractometer (Bruker) with a CU Kα source. The measurements covered scattering angles from 20 to 80° with a step size of 0.05°.

SEM images were acquired by using a JEOL 7401F instrument with an accelerating voltage of 10 kV. SEM-based EDX analysis was conducted with a Bruker XFLASH 4010 instrument at an accelerating voltage of 15 keV.

TEM (bright field) images were acquired using a conventional TECNAI $G^2$20 S-TWIN (FEI/TFS company) with LaB6 electron source, operating at 200 kV accelerating voltage, equipped with a 2 × 2k US1000 CCD camera (Gatan Inc.). The HAADF-STEM images with a detection angle of 54-220 mrad and EDX analysis were performed on a probe Cs-corrected JEM-ARM300F2 (JEOL Ltd.), with a cold-FEG electron source, operated at 200 and 300 kV. The instrument is equipped with a windowless dual SDD EDX system (JEOL Ltd.) with a solid angle of 2.2 sr. For EDX data acquisition and evaluation, the supplied software AnalysisStation was used. The TEM and STEM samples were prepared by dispersing the catalysts in ethanol with ultrasonication and drop-cast onto 300 mesh lacey carbon Cu grids (Plano).

The signal-to-noise ratio of EDX mappings from SEM and TEM were improved by the use of a 5 × 5 Gaussian low-pass filter for visual reasons.

XRF measurements were performed on an S8 Tiger XRF instrument (Bruker) with a Rh X-ray tube.

XPS measurements were performed with a ThermoScientific K Alpha+ X-ray Photoelectron Spectrometer. All samples were analyzed using a microfocused, monochromated Al K α X-ray source (1486.68 eV; 400 μm spot size), while the analyzer had a pass energy of 50 eV. To prevent any localized charge buildup during analysis, the K-Alpha+ charge compensation system was employed at all measurements. The peak fitting was performed by using CasaXPS.

XAS at the Ni K-edge and Ir L_3-edge were performed at beamline KMC-3 at the BESSY-II synchrotron (Helmholtz Center Berlin, Germany; 300 mA top-up mode of the storage ring) as described earlier,[50] using a setup including a Si[111] double-crystal monochromator, a 13-element energy-resolving Si-drift detector (RaySpec), and DXP-XMAP pulse-processing electronics (XIA).[51] Samples were held in a liquid-helium cryostat (Oxford) at 20 K. The energy axis of the monochromator was calibrated (accuracy ±0.1 eV) by using the K-edge spectrum of a nickel metal foil (fitted reference energy of 8333 eV in the first derivative spectrum). The spot size on the samples was ca. 2 mm × 4 mm (vertical × horizontal) as set by a focusing mirror and slits. X-ray fluorescence spectra were collected using a continuous monochromator-scan mode (scan duration of ~7 min, 1 scan per sample spot). 2−3 scans were averaged for signal-to-noise ratio improvement. XAS data were processed (dead-time correction, background subtraction, normalization) to yield XANES and EXAFS spectra using our earlier described procedures and in-house software.[52] Both fluorescence- and absorption-detected spectra were collected; the fluorescence signal was corrected for flattening due to (high) sample absorption; and both data sets were averaged to obtain the EXAFS spectra that were subjected to quantitative analysis. k^3-weighted EXAFS spectra were simulated with in-house software and phase functions from FEFF8 ($S_0^2 = 1$).[53]

Conductivity measurements were carried out by using a homemade setup (Figure S17).

Electrochemical Measurements in RDE. The electrochemical characterizations were carried out at room temperature in a three-electrode cell with a Pt mesh as the counter electrode (CE), a gold RDE with a diameter of 5 mm (area: 0.196 cm^2) as the working electrode (WE), and an Hg/Hg_2SO_4 as the reference electrode (RE). SP-200 and VSP potentiostats (Bio-Logic Science Instruments) were used for the measurements. All measurements were performed in N_2-saturated 0.05 M H_2SO_4 solution (diluted from 98% H_2SO_4 with Milli-Q water) and repeated three times for each catalyst. All measured potentials were referred to a reversible hydrogen electrode (RHE). RE was regularly calibrated using a homemade RHE setup. Catalyst ink was prepared using a certain amount of catalyst (ca. 8−9 mg), 7.5 mL of Milli-Q water, 2.5 mL of isopropanol, and a certain amount of Nafion ionomer solution (15 wt % of the catalyst film). The ink was dispersed using an ultrasonic horn sonifier (Branson Sonifier 150) for 15 min in an ice bath; 10 μL of the ink was drop-casted onto the WE and was dried at 60 °C for 9 min in air. The Ir loading on the electrode was 17.8 μg_{Ir} cm^{-2}.

The OER activity measurements were performed via a linear sweep voltammetry (LSV) from 1.0 V vs RHE to the voltage AT 10 mA cm^{-2} with a scan rate of 5 mV s^{-1}. The ASTs were performed via SWV between 0.6 V vs RHE and 1.6 V vs RHE with a step duration of 3 s for 2500 and 5000 cycles. Chronopotentiometry at a current density of 10 mA cm^{-2} for 20 h was also performed as the stability test (Scheme S1).

All potentials were iR corrected using the equation $E_{\text{corrected}} = E_{\text{measured}} - iR$, where i is the current and R is the ohmic resistance measured by potentiostatic electrochemical impedance spectroscopy (PEIS). MA was calculated by dividing the current at a certain potential by the mass of iridium on the electrode. SA was calculated by dividing the current at a certain potential by the average charge integrated from anodic and cathodic scans of CVs in the potential range of 0.4 to 1.3 V vs RHE, at a scan rate of 50 mV/s.

SFC-ICP−MS Measurements. *Ink Preparation.* All samples were dispersed in a mixture of IPA/H_2O (7:1 V/V). Nafion ionomer solution (Perfluorinated resin solution with Nafion 1100 W, Sigma) was added to suppress catalyst detachment (ionomer/catalyst = 4.5:1 w/w). The homogenization of the dispersion took place in an ice bath with an ultrasonic horn (Branson Ultrasonics SFX150). Then, 0.1 M KOH was added to the dispersion to adjust the pH to 11 by means of a HI5521 benchtop meter (Hanna Instruments). The duration of the ultrasonication was 15 min with constant pulsation of 4 s on and 2 s off steps. To drop-cast the homogeneous dispersion, glassy carbon (GC, 5 × 5 cm^2, HTW Sigradur G) was polished using a Struers LaboForce-100 polishing machine and rinsed with acetone and water subsequently. Aliquots of 0.2 μL[54] or 0.3 μL were deposited onto the clean surface of the GC substrate and dried at ambient air temperature. The catalyst loading of a single spot was approximately 10 μg_{Ir} cm^{-2}. This was determined with a Keyence VK-X250 profilometer.

Electrochemical Characterization and Stability Measurements. The experiments were performed with an SFC with downstream detection by ICP−MS (Agilent 7900 ICP−MS, Agilent). 0.1 M $HClO_4$ was prepared as the electrolyte and was purged with Ar to avoid the accumulation of ambient oxygen on the catalyst surface. The electrolyte was supplied by a peristaltic pump (Masterflex Reglo ICC, Ismatec) into the SFC and sucked into the mass spectrometer by its peristalsis at controlled mixing with the internal standard solution (ISTD, ratio 2:1). The calibration of the ICP−MS was carried out daily with standard solutions of the concentrations 0.5, 1, and 5 ppb. As the ISTD, ^{187}Re, ^{72}Ge, and ^{45}Sc were used for ^{193}Ir, ^{60}Ni, and ^{47}Ti, respectively.

The electrochemical measurements were conducted with a potentiostat/galvanostat/ZRA (Reference 620, Gamry Instruments). As for the RE and CE, a RHE (Hydroflex Mini, Gaskatel) and a GC rod (Sigradur G, d = 1.6 mm, HTW) were selected, respectively. The standard potential of the RHE was regularly obtained against a Pt wire in 0.1 M $HClO_4$ (Ultrex, J.T.Baker) solution at continuous H_2 flow in a simple benchmark cell for this purpose. The drop-cast catalyst spots were applied as the working electrode on the GC backing electrode. The electrochemical protocol consisted of: (1) open-circuit potential (OCP) for 120 s, (2) LSV between 0.8 and 1.7 V vs RHE at a scan rate of 20 mV s^{-1}, (3) potentiostatic hold at 0.8 V vs RHE for 300 s, (4) galvanostatic hold at 1 mA cm^{-2} for 600 s, (5) potentiostatic hold at 0.8 V vs RHE for 300 s, and 6. OCP for 120 s. Finally, PEIS was applied to assess the impedance of the electrolyte. Impedance spectra were recorded between 100 and 1 kHz using a sinusoidal excitation signal with an amplitude of 10 mV vs the OCP of each measurement and an initial impedance guess of 50 Ω. Each catalyst material was investigated at least at three distinct spots. The S-number is defined as the ratio between the amount of evolved oxygen (calculated from Q_{total}) and the amount of dissolved iridium (extracted from ICP−MS data). S-number = n_{O_2}/n_{Ir}. The S-number describes how many oxygen molecules are formed per one iridium atom dissolved in the electrolyte.

MEA Measurements. The measurements were performed by using a Greenlight test station with a 5 cm^2 PEMWE single-cell setup. The ink of the anode catalysts was prepared by dispersing the catalyst and 5 wt % Nafion solution in a mixture of isopropanol and Milli-Q water (isopropanol/H_2O = 99:1) using UP200 St (Hielscher Ultrasonics GmbH). The Nafion to catalyst weight ratio was kept at 12 wt %. The commercial cathode catalyst (Elyst Pt50) was used as the cathode catalyst. The ink preparation of the cathode catalyst was the same as the anode catalyst, only with a different Nafion to catalyst weight ratio of 20 wt %. The decals were prepared using ExactaCoat from Sono-Tek corporation. A certain amount of ink was sprayed on the fluorinated ethylene propylene (FEP) foil covered with a 5 cm^2 mask at 90 °C. The catalyst coated membranes (CCM) was prepared by hot pressing the coated FEP foils onto Nafion 212 (50 μm) at 155 °C at a pressure of 2.4 MPa for 3 min. Then, the CCM was cooled to RT. The catalyst loading was determined by weighing the decals before and after the transfer step. The aiming loading of Ir on the membrane was around 2.0 mg_{Ir}/cm^2 for Elyst75 and ca. 0.3 mg_{Ir}/cm^2 for as-synthesized catalysts. The loading of Pt on the PTL was 0.1 mg_{pt}/cm^2. Carbon paper was used as the PTL on the cathode side, and Pt coated Ti PTL was used in the anode side. The measurements were carried out at 80 °C under ambient pressure in pure water. Before the actual measurement, a short break-in (1 h @ 1 A/cm^2) was performed followed by five CVs (0.05−1.35 V, 50 mV/s, hydrogen at cathode) and a galvanostatic staircase voltammetry. At the end of each current step, a galvanostatic impedance spectrum was recorded in order to determine the HFR at each step. The combination of CV and galvanostatic staircase voltammetry was performed three consecutive times. The final curve was obtained by averaging of the 3 curves. Chronopotentiometric measurements were conducted as a stability test at a current density of 2 A cm^{-2} for 100 h.

■ ASSOCIATED CONTENT

Supporting Information

The Supporting Information is available free of charge at https://pubs.acs.org/doi/10.1021/acscatal.4c06385.

> Schematic of the electrochemical protocol for RDE; additional SEM, TEM, EDX mappings, and STEM; additional XRD patterns; compositional details determined by XRF, XPS, and EDX; Ir L_3-edge and Ni K-edge XANES, simulations of EXAFS data, and EXAFS fitting results; XPS spectra of Ni 2p and O 1s, additional XPS spectra of Ir 4f and Ir peak fitting parameters; conductivity measurements setup and results; additional electrochemical activity and stability measurements results; additional SFC-ICP−MS results; and MEA setup and additional MEA results (PDF)

■ AUTHOR INFORMATION

Corresponding Author

Peter Strasser − *Department of Chemistry, Technische Universität Berlin, Berlin 10623, Germany*; orcid.org/0000-0002-3884-436X; Email: pstrasser@tu-berlin.de

Authors

Jiaqi Kang − *Department of Chemistry, Technische Universität Berlin, Berlin 10623, Germany*

Xingli Wang − *Department of Chemistry, Technische Universität Berlin, Berlin 10623, Germany*

Sebastian Möhle − *Department of Chemistry, Technische Universität Berlin, Berlin 10623, Germany*

Shima Farhoosh − *Department of Chemistry, Technische Universität Berlin, Berlin 10623, Germany; Department of Physics, Freie Universität Berlin, Berlin 14195, Germany*

Miklós Márton Kovács − *Helmholtz Institute Erlangen-Nürnberg for Renewable Energy (IET-2), Forschungszentrum Jülich GmbH, Erlangen 91058, Germany; Department of Chemical and Biological Engineering, Friedrich-Alexander-Universität Erlangen-Nürnberg, Erlangen 91058, Germany*; orcid.org/0000-0001-8653-7906

Johannes Schmidt − *Department of Chemistry, Technische Universität Berlin, Berlin 10623, Germany*

Liang Liang − *Department of Chemistry, Technische Universität Berlin, Berlin 10623, Germany*; orcid.org/0009-0006-1768-6960

Matthias Kroschel − *Department of Chemistry, Technische Universität Berlin, Berlin 10623, Germany*

Sören Selve − *Center for Electron Microscopy (ZELMI), Technische Universität Berlin, Berlin 10623, Germany*

Michael Haumann − *Department of Physics, Freie Universität Berlin, Berlin 14195, Germany*

Dominik Dworschak − *Helmholtz Institute Erlangen-Nürnberg for Renewable Energy (IET-2), Forschungszentrum Jülich GmbH, Erlangen 91058, Germany*; orcid.org/0000-0002-7585-767X

Holger Dau − *Department of Physics, Freie Universität Berlin, Berlin 14195, Germany*; orcid.org/0000-0001-6482-7494

Complete contact information is available at: https://pubs.acs.org/10.1021/acscatal.4c06385

Author Contributions

The manuscript was written through contributions of all authors. All authors have given approval to the final version of the manuscript.

Notes

The authors declare no competing financial interest.

■ ACKNOWLEDGMENTS

Financial support by the Federal Ministry of Education and Research (Bundesministerium für Bildung und Forschung, BMBF) in the collaborative research project H_2Giga (project number: 03HY108D and 03HY108A) is gratefully acknowledged by the authors. The authors thankfully acknowledge financial support from the German Research Foundation (Deutsche Forschungsgemeinschaft, DFG) under grant STR-596/21-1. STEM Analysis is funded by DFG under the research project DFG-INST 131/789-1 FUGG (project number: 403371556). We thank the Center for Electron Microscopy (ZELMI) at TU Berlin in the context of the Alliance Center Electron Microscopy (ACEM) for support in acquisition (and analysis) of the data. The ACEM is funded under the Excellence Strategy of the Federal Government and the Länder by the Berlin University Alliance (BUA). The authors acknowledge support from the Cluster of Excellence "UniSysCat" funded by DFG under EXC2008-390540038.

REFERENCES

(1) Pellow, M. A.; Emmott, C. J. M.; Barnhart, C. J.; Benson, S. M. Hydrogen or batteries for grid storage? A net energy analysis. *Energy Environ. Sci.* **2015**, *8* (7), 1938−1952.

(2) Clapp, M.; Zalitis, C. M.; Ryan, M. Perspectives on current and future iridium demand and iridium oxide catalysts for PEM water electrolysis. *Catal. Today* **2023**, *420*, 114140.

(3) Nong, H. N.; Gan, L.; Willinger, E.; Teschner, D.; Strasser, P. IrOx core-shell nanocatalysts for cost- and energy-efficient electrochemical water splitting. *Chem. Sci.* **2014**, *5* (8), 2955−2963.

(4) Olabi, A. G.; Wilberforce, T.; Abdelkareem, M. A. Fuel cell application in the automotive industry and future perspective. *Energy* **2021**, *214*, 118955.

(5) Gao, G.; Sun, Z.; Chen, X.; Zhu, G.; Sun, B.; Liu, S.; Yamauchi, Y. Recent advances in Ru/Ir-based electrocatalysts for acidic oxygen evolution reaction. *Appl. Catal., B* **2024**, *343*, 123584.

(6) Bernt, M.; Hartig-Weiß, A.; Tovini, M. F.; El-Sayed, H. A.; Schramm, C.; Schröter, J.; Gebauer, C.; Gasteiger, H. A. Current Challenges in Catalyst Development for PEM Water Electrolyzers. *Chem. Ing. Tech.* **2020**, *92* (1−2), 31−39.

(7) Reier, T.; Nong, H. N.; Teschner, D.; Schlögl, R.; Strasser, P. Electrocatalytic Oxygen Evolution Reaction in Acidic Environments − Reaction Mechanisms and Catalysts. *Adv. Energy Mater.* **2017**, *7*, 1601275.

(8) Böhm, D.; Beetz, M.; Schuster, M.; Peters, K.; Hufnagel, A. G.; Döblinger, M.; Böller, B.; Bein, T.; Fattakhova-Rohlfing, D. Efficient OER Catalyst with Low Ir Volume Density Obtained by Homogeneous Deposition of Iridium Oxide Nanoparticles on Macroporous Antimony-Doped Tin Oxide Support. *Adv. Funct. Mater.* **2020**, *30* (1), 1906670.

(9) Oakton, E.; Lebedev, D.; Povia, M.; Abbott, D. F.; Fabbri, E.; Fedorov, A.; Nachtegaal, M.; Copéret, C.; Schmidt, T. J. IrO2-TiO2: A High-Surface-Area, Active, and Stable Electrocatalyst for the Oxygen Evolution Reaction. *ACS Catal.* **2017**, *7* (4), 2346−2352.

(10) Pham, C. V.; Bühler, M.; Knöppel, J.; Bierling, M.; Seeberger, D.; Escalera-López, D.; Mayrhofer, K. J. J.; Cherevko, S.; Thiele, S. IrO2 coated TiO2 core-shell microparticles advance performance of low loading proton exchange membrane water electrolyzers. *Appl. Catal., B* **2020**, *269*, 118762.

(11) Nhan Nong, H.; Willinger, E.; Teschner, D.; Strasser, P. IrOx core-shell nanocatalysts for cost- and energy efficient electrochemical water splitting. *Chem. Sci.* **2014**, *5*, 2955−2963.

(12) Sasaki, K.; Kuttiyiel, K. A.; Barrio, L.; Su, D.; Frenkel, A. I.; Marinkovic, N.; Mahajan, D.; Adzic, R. R. Carbon-Supported IrNi Core−Shell Nanoparticles: Synthesis, Characterization, and Catalytic Activity. *J. Phys. Chem. C* **2011**, *115* (20), 9894−9902.

(13) Shan, J.; Ye, C.; Chen, S.; Sun, T.; Jiao, Y.; Liu, L.; Zhu, C.; Song, L.; Han, Y.; Jaroniec, M.; Zhu, Y.; Zheng, Y.; et al. Short-Range Ordered Iridium Single Atoms Integrated into Cobalt Oxide Spinel Structure for Highly Efficient Electrocatalytic Water Oxidation. *J. Am. Chem. Soc.* **2021**, *143*, 5201−5211.

(14) Chong, L.; Wen, J.; Song, E.; Yang, Z.; Bloom, I. D.; Ding, W. Synergistic Co−Ir/Ru Composite Electrocatalysts Impart Efficient and Durable Oxygen Evolution Catalysis in Acid. *Adv. Energy Mater.* **2023**, *13* (37), 2302306.

(15) Chen, X.; Li, W.; Song, N.; Zhong, M.; Yan, S.; Xu, J.; Zhu, W.; Wang, C.; Lu, X. Electronic modulation of iridium-molybdenum oxides with a low crystallinity for high-efficiency acidic oxygen evolution reaction. *Chem. Eng. J.* **2022**, *440*, 135851.

(16) Wang, F.; Wu, D.; Yamamoto, T.; Toriyama, T.; Matsumura, S.; Nanba, Y.; Koyama, M.; Kitagawa, H. Solid-Solution Alloy Nanoparticles of the Immiscible Ir-Cu System with a Wide Composition Range for Enhanced Electrocatalytic Applications. *Angew. Chem., Int. Ed.* **2018**, *57* (17), 4505−4509.

(17) Hu, W.; Zhong, H.; Liang, W.; Chen, S. Ir-Surface Enriched Porous Ir−Co Oxide Hierarchical Architecture for High Performance Water Oxidation in Acidic Media. *ACS Appl. Mater. Interfaces* **2014**, *6* (15), 12729−12736.

(18) Park, S.; Shviro, M.; Hartmann, H.; Besmehn, A.; Mayer, J.; Stolten, D.; Carmo, M. Nickel Structures as a Template Strategy to Create Shaped Iridium Electrocatalysts for Electrochemical Water Splitting. *ACS Appl. Mater. Interfaces* **2021**, *13* (11), 13576−13585.

(19) Lim, J.; Yang, S.; Kim, C.; Roh, C.-W.; Kwon, Y.; Kim, Y.-T.; Lee, H. Shaped Ir−Ni bimetallic nanoparticles for minimizing Ir utilization in oxygen evolution reaction. *Chem. Commun.* **2016**, *52* (32), 5641−5644.

(20) Shinozaki, K.; Zack, J. W.; Richards, R. M.; Pivovar, B. S.; Kocha, S. S. Oxygen Reduction Reaction Measurements on Platinum Electrocatalysts Utilizing Rotating Disk Electrode Technique: I. Impact of Impurities, Measurement Protocols and Applied Corrections. *J. Electrochem. Soc.* **2015**, *162* (10), F1144.

(21) Lazaridis, T.; Stühmeier, B. M.; Gasteiger, H. A.; El-Sayed, H. A. Capabilities and limitations of rotating disk electrodes versus membrane electrode assemblies in the investigation of electrocatalysts. *Nat. Catal.* **2022**, *5* (5), 363−373.

(22) Nong, H. N.; Reier, T.; Oh, H.-S.; Gliech, M.; Paciok, P.; Vu, T. H. T.; Teschner, D.; Heggen, M.; Petkov, V.; Schlögl, R.; et al. A unique oxygen ligand environment facilitates water oxidation in hole-doped IrNiOx core−shell electrocatalysts. *Nat. Catal.* **2018**, *1* (11), 841−851.

(23) Yoo, H.; Oh, K.; Lee, Y. R.; Row, K. H.; Lee, G.; Choi, J. Simultaneous co-doping of RuO2 and IrO2 into anodic TiO2 nanotubes: A binary catalyst for electrochemical water splitting. *Int. J. Hydrogen Energy* **2017**, *42* (10), 6657−6664.

(24) Fuentes, R. E.; Farell, J.; Weidner, J. W. Multimetallic Electrocatalysts of Pt, Ru, and Ir Supported on Anatase and Rutile TiO2 for Oxygen Evolution in an Acid Environment. *Electrochem. Solid-State Lett.* **2011**, *14* (3), No. E5.

(25) Lee, C.; Shin, K.; Park, Y.; Yun, Y. H.; Doo, G.; Jung, G. H.; Kim, M.; Cho, W.-C.; Kim, C.-H.; Lee, H. M.; et al. Catalyst-Support Interactions in Zr2ON2-Supported IrOx Electrocatalysts to Break the Trade-Off Relationship Between the Activity and Stability in the Acidic Oxygen Evolution Reaction. *Adv. Funct. Mater.* **2023**, *33*, 2301557.

(26) Tran, H. P.; Nong, H. N.; Oh, H.-S.; Klingenhof, M.; Kroschel, M.; Paul, B.; Hübner, J.; Teschner, D.; Strasser, P. Catalyst−Support Surface Charge Effects on Structure and Activity of IrNi-Based Oxygen Evolution Reaction Catalysts Deposited on Tin-Oxide Supports. *Chem. Mater.* **2022**, *34* (21), 9350−9363.

(27) Mazúr, P.; Polonský, J.; Paidar, M.; Bouzek, K. Non-conductive TiO2 as the anode catalyst support for PEM water electrolysis. *Int. J. Hydrogen Energy* **2012**, *37* (17), 12081−12088.

(28) Nakatuka, Y.; Yoshida, H.; Fukui, K.; Matuzawa, M. The effect of particle size distribution on effective zeta-potential by use of the sedimentation method. *Adv. Powder Technol.* **2015**, *26* (2), 650−656.

(29) Wu, G.; Zheng, X.; Cui, P.; Jiang, H.; Wang, X.; Qu, Y.; Chen, W.; Lin, Y.; Li, H.; Han, X.; et al. A general synthesis approach for amorphous noble metal nanosheets. *Nat. Commun.* **2019**, *10* (1), 4855.

(30) Yu, H.; Liao, F.; Zhu, W.; Qin, K.; Shi, J.; Ma, M.; Li, Y.; Fang, M.; Su, J.; Song, B.; et al. Two-Dimensional Amorphous Iridium Oxide for Acidic Oxygen Evolution Reaction. *ChemCatChem* **2023**, *15* (19), No. e202300737.

(31) Pfeifer, V.; Jones, T. E.; Velasco Vélez, J. J.; Massué, C.; Greiner, M. T.; Arrigo, R.; Teschner, D.; Girgsdies, F.; Scherzer, M.; Allan, J.; et al. The electronic structure of iridium oxide electrodes active in water splitting. *Phys. Chem. Chem. Phys.* **2016**, *18* (4), 2292−2296.

(32) Reier, T.; Pawolek, Z.; Cherevko, S.; Bruns, M.; Jones, T.; Teschner, D.; Selve, S.; Bergmann, A.; Nong, H. N.; Schlögl, R.; Mayrhofer, K. J. J.; et al. Molecular Insight in Structure and Activity of Highly Efficient, Low-Ir Ir−Ni Oxide Catalysts for Electrochemical Water Splitting (OER). *J. Am. Chem. Soc.* **2015**, *137*, 13031−13040.

(33) Xu, Y.; Mao, Z.; Zhang, J.; Ji, J.; Zou, Y.; Dong, M.; Fu, B.; Hu, M.; Zhang, K.; Chen, Z.; et al. Strain-modulated Ru-O Covalency in Ru-Sn Oxide Enabling Efficient and Stable Water Oxidation in Acidic Solution. *Angew. Chem., Int. Ed.* **2024**, *63*, No. e202316029.

(34) Lee, S.; Lee, Y.-J.; Lee, G.; Soon, A. Activated chemical bonds in nanoporous and amorphous iridium oxides favor low overpotential for oxygen evolution reaction. *Nat. Commun.* **2022**, *13* (1), 3171.

(35) Zhao, F.; Wen, B.; Niu, W.; Chen, Z.; Yan, C.; Selloni, A.; Tully, C. G.; Yang, X.; Koel, B. E. Increasing Iridium Oxide Activity for the Oxygen Evolution Reaction with Hafnium Modification. *J. Am. Chem. Soc.* **2021**, *143* (38), 15616−15623.

(36) Shinagawa, T.; Garcia-Esparza, A. T.; Takanabe, K. Insight on Tafel slopes from a microkinetic analysis of aqueous electrocatalysis for energy conversion. *Sci. Rep.* **2015**, *5* (1), 13801.

(37) Hu, J.-M.; Zhang, J.-Q.; Cao, C.-N. Oxygen evolution reaction on IrO2-based DSA® type electrodes: kinetics analysis of Tafel lines and EIS. *Int. J. Hydrogen Energy* **2004**, *29* (8), 791−797.

(38) Cherevko, S.; Geiger, S.; Kasian, O.; Mingers, A.; Mayrhofer, K. J. J. Oxygen evolution activity and stability of iridium in acidic media. Part 1. − Metallic iridium. *J. Electroanal. Chem.* **2016**, *773*, 69−78.

(39) Spöri, C.; Briois, P.; Nong, H. N.; Reier, T.; Billard, A.; Kühl, S.; Teschner, D.; Strasser, P. Experimental Activity Descriptors for Iridium-Based Catalysts for the Electrochemical Oxygen Evolution Reaction (OER). *ACS Catal.* **2019**, *9*, 6653−6663.

(40) Regmi, Y. N.; Tzanetopoulos, E.; Zeng, G.; Peng, X.; Kushner, D. I.; Kistler, T. A.; King, L. A.; Danilovic, N. Supported Oxygen Evolution Catalysts by Design: Toward Lower Precious Metal Loading and Improved Conductivity in Proton Exchange Membrane Water Electrolyzers. *ACS Catal.* **2020**, *10* (21), 13125−13135.

(41) Marshall, A.; Børresen, B.; Hagen, G.; Tsypkin, M.; Tunold, R. Preparation and characterisation of nanocrystalline IrxSn1−xO2 electrocatalytic powders. *Mater. Chem. Phys.* **2005**, *94* (2), 226−232.

(42) Bernt, M.; Schramm, C.; Schröter, J.; Gebauer, C.; Byrknes, J.; Eickes, C.; Gasteiger, H. A. Effect of the IrOx Conductivity on the Anode Electrode/Porous Transport Layer Interfacial Resistance in PEM Water Electrolyzers. *J. Electrochem. Soc.* **2021**, *168* (8), 084513.

(43) Böhm, D.; Beetz, M.; Gebauer, C.; Bernt, M.; Schröter, J.; Kornherr, M.; Zoller, F.; Bein, T.; Fattakhova-Rohlfing, D. Highly conductive titania supported iridium oxide nanoparticles with low overall iridium density as OER catalyst for large-scale PEM electrolysis. *Appl. Mater. Today* **2021**, *24*, 101134.

(44) Geiger, S.; Kasian, O.; Ledendecker, M.; Pizzutilo, E.; Mingers, A. M.; Fu, W. T.; Diaz-Morales, O.; Li, Z.; Oellers, T.; Fruchter, L.; et al. The stability number as a metric for electrocatalyst stability benchmarking. *Nat. Catal.* **2018**, *1* (7), 508−515.

(45) Li, N.; Araya, S. S.; Cui, X.; Kær, S. K. The effects of cationic impurities on the performance of proton exchange membrane water electrolyzer. *J. Power Sources* **2020**, *473*, 228617.

(46) Siracusano, S.; Hodnik, N.; Jovanovic, P.; Ruiz-Zepeda, F.; Šala, M.; Baglio, V.; Aricò, A. S. New insights into the stability of a high performance nanostructured catalyst for sustainable water electrolysis. *Nano Energy* **2017**, *40*, 618−632.

(47) Pham, C. V.; Bühler, M.; Knöppel, J.; Bierling, M.; Seeberger, D.; Escalera-López, D.; Mayrhofer, K. J. J.; Cherevko, S.; Thiele, S. IrO2 coated TiO2 core-shell microparticles advance performance of low loading proton exchange membrane water electrolyzers. *Appl. Catal., B* **2020**, *269*, 118762.

(48) Minke, C.; Suermann, M.; Bensmann, B.; Hanke-Rauschenbach, R. Is iridium demand a potential bottleneck in the realization of large-scale PEM water electrolysis? *Int. J. Hydrogen Energy* **2021**, *46* (46), 23581−23590.

(49) Godínez-Salomón, F.; Albiter, L.; Alia, S. M.; Pivovar, B. S.; Camacho-Forero, L. E.; Balbuena, P. B.; Mendoza-Cruz, R.; Arellano-Jimenez, M. J.; Rhodes, C. P. Self-Supported Hydrous Iridium−Nickel Oxide Two-Dimensional Nanoframes for High Activity Oxygen Evolution Electrocatalysts. *ACS Catal.* **2018**, *8* (11), 10498−10520.

(50) Kass, D.; Corona, T.; Warm, K.; Braun-Cula, B.; Kuhlmann, U.; Bill, E.; Mebs, S.; Swart, M.; Dau, H.; Haumann, M.; et al. Stoichiometric Formation of an Oxoiron(IV) Complex by a Soluble Methane Monooxygenase Type Activation of O2 at an Iron(II)-Cyclam Center. *J. Am. Chem. Soc.* **2020**, *142* (13), 5924−5928.

(51) Chernev, P.; Fischer, S.; Hoffmann, J.; Oliver, N.; Assunção, R.; Yu, B.; Burnap, R. L.; Zaharieva, I.; Nürnberg, D. J.; Haumann, M.; et al. Light-driven formation of manganese oxide by today's photosystem II supports evolutionarily ancient manganese-oxidizing photosynthesis. *Nat. Commun.* **2020**, *11* (1), 6110.

(52) Dau, H.; Liebisch, P.; Haumann, M. X-ray absorption spectroscopy to analyze nuclear geometry and electronic structure of biological metal centers—potential and questions examined with special focus on the tetra-nuclear manganese complex of oxygenic photosynthesis. *Anal. Bioanal. Chem.* **2003**, *376* (5), 562−583.

(53) Ankudinov, A. L.; Ravel, B.; Rehr, J. J.; Conradson, S. D. Real-space multiple-scattering calculation and interpretation of x-ray-absorption near-edge structure. *Phys. Rev. B:Condens. Matter Mater. Phys.* **1998**, *58* (12), 7565−7576.

(54) Zlatar, M.; Escalera-López, D.; Rodríguez, M. G.; Hrbek, T.; Götz, C.; Mary Joy, R.; Savan, A.; Tran, H. P.; Nong, H. N.; Pobedinskas, P.; et al. Standardizing OER Electrocatalyst Benchmarking in Aqueous Electrolytes: Comprehensive Guidelines for Accelerated Stress Tests and Backing Electrodes. *ACS Catal.* **2023**, *13*, 15375−15392.